

Research on Liquid Water Distribution in PEMFC Cathode Porous Media

Hongjian Liu¹, Guodong Zhang¹, Zeting Yu¹, Da Li¹, Guihua Wang¹, Congkang Wang², Shuzhan Bai^{1,*}, Guoxiang Li^{1,**}

¹ School of Energy and Power Engineering, Shandong University, Jinan 250061, China;

² Suzhou Foresight Energy Technology Co., Ltd., Suzhou 215300, China)

*E-mail: baishuzhan@sdu.edu.cn, liguox@sdu.edu.cn

Received: 2 March 2020 / Accepted: 22 April 2020 / Published: 10 June 2020

A mass transfer model that modifies the Bruggeman equation for oxygen diffusion in the gas diffusion layer (GLD) has been proposed and validated by experiments. The experimental results indicate that the modified model can accurately simulate the actual working conditions of proton exchange membrane fuel cell (PEMFC) during concentration polarization. The differences of numerical simulation results between before and after modification are further compared, and the distribution characteristics of liquid water in porous media are explored. The results reveal that liquid water saturation and oxygen concentration predicted by the traditional Bruggeman equation are both higher, and for different models the smaller the value of β (or the absolute value of α) is, the more the liquid water will be. The liquid water is accumulated and oxygen mass transfer resistance is enhanced due to increased current density. The reaction rate decreases during concentration polarization, and the generation rate of liquid water slows down accordingly. The growth rate of liquid water and the decrease rate of oxygen concentration under rib are larger than those under channel. The liquid water accumulates much more significantly under rib than under channel at a common working voltage of around 0.55 V. As GDL porosity decreases, liquid water under channel increases almost linearly while the change of liquid water saturation under rib exhibits a parabolic trend. On the whole, liquid water is slightly saturated when porosity is greater than 0.65. Smaller GDL pore size will considerably increase ‘flooding’ risk, and thinner GDL thickness is beneficial to the removal of liquid water.

Keywords: PEMFC; Liquid water distribution; Porous media; Numerical simulation

1. INTRODUCTION

Featuring in high energy density, fast starting speed, strong endurance, efficient energy conversion and environmentally-friendly emission, proton exchange membrane fuel cells (PEMFCs) are considered to be one of the most promising vehicle power sources in the future [1-3]. The low-

temperature proton exchange membrane fuel cell (LT-PEMFC) works at a temperature of less than 100 °C, thus some of the water that is generated in the fuel cells is in a liquid phase. If excess liquid water is not timely discharged, the continuously accumulated liquid water will block mass transfer channel and affect gas transportation and distribution. The substances covered on the surface of the catalyst will reduce the utilization rate of the catalyst and cause a sharp decline or even failure in the cell performance, resulting in so-called 'liquid water flooding'. The greater the power density is, the more likely the problem will occur. Therefore, in order to further increase the power density and accelerate the commercialization of PEMFC, it is of great importance to effectively prevent 'flooding' from happening.

Scholars have conducted lots of simulation and experimental researches on liquid water distribution of PEMFC. The numerical models range from simple 1D (one-dimensional) single-phase flow to a complex 3D (three-dimensional) multi-phase flow, which are used to predict 'flooding' or study its influence on cell performance. Djilali et al. [4] developed a non-isothermal and non-isobaric 1D model of PEMFC water transportation and analyzed fuel cell performance and water transport in certain range of working current. The results indicated that the non-uniform distribution of temperature and pressure had a significant impact on predicting liquid water in the gas diffusion layer. Rowe et al. [5] developed a 1D non-isothermal model of PEMFC, and investigated the influences of various operating conditions on the cell performance. It was found that the temperature distribution of PEMFC was affected by the change of water phase in the electrode. The 1D model can demonstrate the influences of different working conditions on PEMFC performance better without considering the multi-dimensional effect, so it is suitable for studying unidirectional mass transfer. Lee et al. [6] developed a 2D (two-dimensional) pore-network model to study the water transport in the gas diffusion layer of PEMFC. The numerical results showed that the water transport in the gas diffusion layer was strongly influenced by capillary pressure. Sun et al. [7] developed a two-phase model based on the model of mixture flow to study the influences of operating temperature, pressure and humidity on the transportation of oxygen, vapor and liquid water. The 2D numerical simulations of PEMFC mostly involve the influences of different operating conditions on the cell performance, while little attention is paid to the detailed characteristics of liquid water distribution in porous media. In recent years, more and more 3D models [8-11] are used in PEMFC numerical simulations, but there are common problems such as larger amount of calculation and difficulty in convergence. By contrast, the 2D model not only owns a smaller amount of calculation, but also completely displays the detailed characteristics of liquid water distribution, thus facilitating the comparison on the differences of liquid water distribution between under channel and under rib. In terms of experiments, Banerjee et al. [12] used X-ray imaging technology to study the similarities and differences of different gas diffusion layer microstructures and droplet aggregation behavior. Ge et al. [13] used synchrotron radiation X-ray imaging to measure the penetration behavior of water droplets in the microporous layer, and input the results of measurement to the 1D model. Cho et al. [14] used neutron imaging technology to evaluate the formation and transportation of liquid water in the serpentine flow field.

The 'flooding' in the porous media is often more complicated than that in the channels due to the clogging of water liquid in the pores. Since water is mainly produced on the cathode side, it is particularly important to study the liquid water in the porous media of the cathode. Although lots of researches have been carried out on water management, less attention has been paid to the detailed characteristics of the

liquid water distribution in the cathode porous media, and there is less modeling for the cathode porous media area.

In order to further improve PEMFC water management and prevent ‘flooding’ from happening, a 2D, two-phase, isothermal model of the cathode porous media area is established in this study. The Bruggeman equation for oxygen diffusion in this model is modified, and the reliability of the modified model is verified by experiments. Aiming at the liquid water distribution characteristics in porous media under low voltage (high current density), this study also further explores the relationship between liquid water and concentration polarization and investigates the influences of various working conditions and GDL structural characteristics on the liquid water distribution, striving to provide guidance for optimizing PEMFC water management.

2. EXPERIMENTAL METHOD

2.1. Computational domain of numerical model

The computational domain of cathode porous media is shown in Fig. 1, including gas diffusion layer (GDL) and catalyst layer (CL). In this study, in order to improve the efficiency of calculation, symmetrical boundary conditions are used, and upper boundary of GDL is channel width (half) and rib width (half) combined.

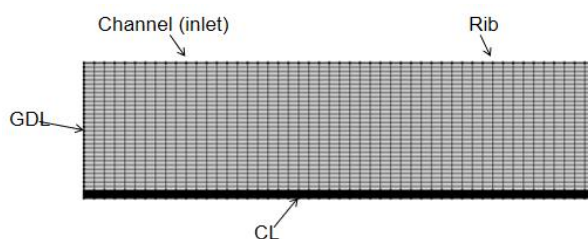


Figure 1. Computational domain.

2.2. Assumptions

- (1) Ideal gas law is applied to all the gas species.
- (2) The PEMFC is operated at steady state.
- (3) Isotropic material properties are considered.
- (4) Mass transfer of gas species adopts Maxwell-Stefan equation.
- (5) No compression of porous media through rib.
- (6) Catalyst structure uses spherical agglomerate model [15], assuming each spherical agglomerate include solid electrode (Pt/C), electrolyte (ionic polymer) and outer liquid water film, from inside to outside, the microstructure is shown in Fig. 2.

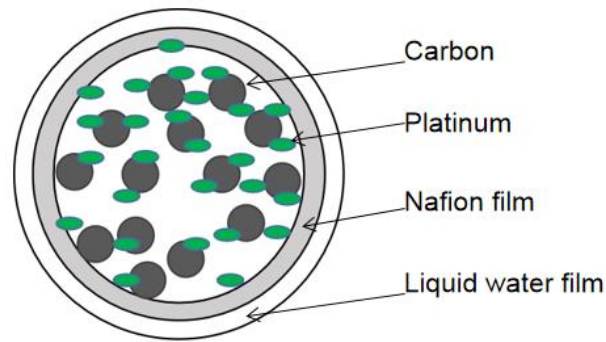


Figure 2. Spherical agglomerate catalyst model [15]

2.3. Governing equations

In this study, the two-fluid model is used to establish numerical model of PEMFC. In the numerical simulation, gas phase governing equation and liquid phase governing equation need to be solved separately. Gas phase (hydrogen, oxygen, water vapor, and nitrogen) is solved with the mass conservation equation, momentum conservation equation, energy conservation equation (gas phase and liquid phase are shared) and component diffusion equation. Liquid phase is solved with liquid water transport equation. Charge conservation equation and electrode kinetic equation are also needed to be solved.

2.3.1. Mass conservation equation

At steady state, mass conservation in porous media is described by the continuity equation:

$$\nabla \rho u = Q_m \tag{1}$$

where ρ is gas mixture density, which is given by Eq. (2); u is velocity vector, Q_m is mass source term; ∇ is differential operator, $\frac{d}{dx} + \frac{d}{dy} + \frac{d}{dz}$.

$$\rho = \frac{p \sum_{i=1}^n x_i M_i}{RT} \tag{2}$$

where p is working pressure, T is working temperature, x_i is the mole fraction of each component, M_i is the mole mass of each component, R is gas constant.

2.3.2. Momentum conservation equation

Using Navier-Stokes equation to describe velocity and pressure variation in porous media:

$$\nabla \cdot (\rho u u) = -\nabla p + \nabla \cdot (\mu \nabla u) + R_u \tag{3}$$

where the term on the left of the equation refers to convection, the former two terms on the right of the equation refer to diffusion, and the last term refers to momentum source term. μ is fluid viscosity, which is given by Eq. (4) [16]:

$$\mu_m = \frac{\sum_{i=1}^n x_i \mu_i M_i^{0.5}}{\sum_{i=1}^n x_i M_i^{0.5}} \quad (4)$$

As velocity and velocity gradient in porous media is relatively small, fluid inertia and viscosity can be neglected, thus momentum equation is simplified by Darcy's law:

$$u = -\frac{\kappa}{\mu} \nabla p \quad (5)$$

where κ is porous media relative permeability.

2.3.3. Energy conservation equation

For the steady-state model, the energy conservation in any region of PEMFC can be described as follows:

$$(\rho c_p)_{eff} (u \nabla T) = \nabla (k_{eff} \nabla T) + S_e \quad (6)$$

where c_p is the specific heat capacity of the mixture, k is the thermal conductivity, S_e is the energy source term. The subscript *eff* represents the effectivity of the porous media [17]:

$$(\rho c_p)_{eff} = (1 - \varepsilon) \rho_s c_{p,s} + \varepsilon \rho c_p \quad (7)$$

$$k_{eff} = -2k_s + \left[\frac{\varepsilon}{2k_s + k} + \frac{1 - \varepsilon}{3k_s} \right]^{-1} \quad (8)$$

where ε is porosity of porous media, ρ_s 、 $c_{p,s}$ 、 k_s represents density, specific heat capacity and thermal conductivity of solid mixture respectively.

2.3.4. Charge conservation equation

To describe ion transfer balance (In the CL) and electron transfer balance (In the CL and GDL):

$$\nabla \cdot (\sigma_s \nabla \phi_s) = j \quad (9)$$

$$\nabla \cdot (\sigma_m \nabla \phi_m) = -j \quad (10)$$

where ϕ_s is electric potential, ϕ_m is ionic potential, j is transfer current density. σ_s is effective conductivity of electron, given in Eq. (11); σ_m is effective conductivity of ion given by Eq. (12) :

$$\sigma_s = \sigma_i (\varepsilon_{Pt/C})^{1.5} \quad (11)$$

$$\sigma_m = (0.005139\lambda - 0.00326) \exp\left[1268\left(\frac{1}{303} - \frac{1}{T}\right)\right] \quad (12)$$

where $\varepsilon_{Pt/C}$ is the ratio of platinum to carbon in the catalyst, and in Eq. (12), λ is water content, given in Eq. (13):

$$\lambda = \begin{cases} 0.043 + 17.81\alpha_{H_2O} - 39.85\alpha_{H_2O}^2 + 36.0\alpha_{H_2O}^3 & \alpha_{H_2O} < 1 \\ 14.0 + 1.4(\alpha_{H_2O} - 1) & 1 \leq \alpha_{H_2O} \leq 3 \\ 16.8 & \alpha_{H_2O} > 3 \end{cases} \quad (13)$$

where α_{H_2O} is water activity, given in Eq. (14):

$$\alpha_{H_2O} = x_{H_2O} \frac{p}{p_{sat}} + 2s \quad (14)$$

where x_{H_2O} is mole fraction of water vapor; p_{sat} is vapor saturation pressure, given in Eq. (15); s is liquid water saturation, which is defined by the ratio of liquid water volume to total porous volume, using the weighted average method of reference [18] for the calculation of liquid water saturation.

$$p_{sat} = 9.531 \times 10^{-4}(T - 237)^4 - 3.123 \times 10^{-2}(T - 237)^3 + 3.451(T - 237)^2 + 20.96(T - 237) + 611.0 \quad (15)$$

2.3.5. Electrode kinetic equation

Electrochemical reaction takes place in the CL, Butler-Volmer equation that describes activation polarization and concentration polarization is given by:

$$i_c = a_{Pt/C}^{eff} i_0 \frac{p_{O_2}}{H_{O_2} c_{O_2}^{ref}} \left[\exp\left(\frac{-\alpha_c F \eta_c}{RT}\right) - \exp\left(\frac{(1-\alpha_c) F \eta_c}{RT}\right) \right] \quad (16)$$

where $a_{Pt/C}^{eff}$ is the effective specific area of the CL, i_0 is the exchange current density, p_{O_2} is partial pressure of oxygen, $c_{O_2}^{ref}$ is reference oxygen concentration, H_{O_2} is Henry's law constant of oxygen, α_c is cathode transfer coefficient, F is Faraday constant. The overpotential η_c is defined as the potential difference of ϕ_s , ϕ_m , and cathode equilibrium potential ϕ_i^{eq} , as shown in Eq. (17):

$$\eta_c = \phi_s - \phi_m - \phi_i^{eq} \quad (17)$$

2.3.6. Component diffusion equation

Using Maxwell-Stefan mass transfer equation to describe diffusion and convection:

$$\nabla \cdot \left[-\rho \omega_i \sum_{j=1}^n D_{ij}^{eff} \left\{ \frac{M_n}{M_j} (\nabla \omega_j + \omega_j \frac{\nabla M_n}{M_n}) + (x_j - \omega_j) \frac{\nabla p}{p} \right\} + \omega_i \rho u \right] = R_i \quad (18)$$

where D_{ij}^{eff} is effective diffusion coefficient of binary gas in porous media, which is a function of effective porosity ε^{eff} , and the relationship is given by Bruggeman equation [19], where 1.5 is the Bruggeman correction factor, as shown in Eq. (19). D_{ij} is the diffusion coefficient of binary gas, given by Eq.(20) ~ Eq.(22); M_j is the mole mass of each component, M_n is the average mole mass, as shown in Eq. (23). ω_i , ω_j and x_j is the mass fraction and mole fraction of each component respectively, R_i is the source term of each component.

$$D_{ij}^{eff} = D_{ij} (\varepsilon^{eff})^{1.5} \quad (19)$$

$$D_{O_2-H_2O} = 0.282 \times 10^{-4} (T / 308.1)^{1.5} \quad (20)$$

$$D_{O_2-N_2} = 0.22 \times 10^{-4} (T / 293.2)^{1.5} \quad (21)$$

$$D_{H_2O-N_2} = 0.256 \times 10^{-4} (T / 307.5)^{1.5} \quad (22)$$

$$M_n = \sum_{j=1}^n x_j M_j \quad (23)$$

where ε^{eff} is effective porosity of porous media, as given in Eq. (24):

$$\varepsilon^{eff} = \varepsilon(1-s) \quad (24)$$

2.3.7. Liquid water transport equation

Applying volume average theory to the continuity equation, and apply Darcy's law to liquid phase and vapor phase, thus the liquid water transport equation can be described as follows::

$$\nabla \cdot (\rho_w^l D_c \nabla s - \frac{\rho_w^l k_r^l \mu_w^s}{k_r^s \mu_w^l} u^s) = M_w S_w^l \quad (25)$$

where ρ_w^l is liquid water density, M_w is mole mass of water, μ_w^s and μ_w^l are kinetic viscosity of vapor and liquid water respectively, k_r^s and k_r^l are relative permeability of vapor and liquid water respectively, D_c is diffusion coefficient, as presented in Eq. (26) [20]:

$$D_c = -\frac{k_r^l}{\mu} \sigma \cos(\theta_c) (\varepsilon^{eff} k_p)^{\frac{1}{2}} \frac{dJ(s)}{ds} \quad (26)$$

where σ is surface tension, θ_c is contact angle, k_p is relative permeability, $J(s)$ is Leverett function [21].

Besides, the model also takes net water transport through proton exchange membrane into consideration. Therefore, source term of vapor in the CL is reaction generation, net water transportation and phase change combined, as shown in Eq. (27):

$$S_w^v = R_{H_2O} (1+2x) - S_w^l \quad (27)$$

where x is net water transport coefficient through the membrane.

The source terms involved of above equations are shown in Table 1 and Table 2.

2.4. Bruggeman equation modification

At present, almost all PEMFC numerical models have adopted the Bruggeman equation [22] to predict gas diffusion in porous media, as shown in Eq. (19). Bruggeman equation can also be written as Eq. (28) and Eq. (29) combined:

$$D_{ij}^{eff} = \frac{\varepsilon}{\tau} (1-s)^\beta \cdot D_{ij} \quad (28)$$

$$\tau = \varepsilon^\alpha \quad (29)$$

where α is parameter related to pore distortion of the dry GDL, and β is parameter related to liquid water distribution of the aqueous GDL, which are two important parameters determining the

effective gas diffusion coefficient. α represents the pore distortion of the porous media, and the greater the absolute value of α is, the larger the resistance of gas diffusion will be; β represents the influence of liquid water on gas diffusion, the greater the value of β is, the larger the influence of liquid water will be. So far, almost all PEMFC numerical simulations have used the traditional Bruggeman equation and parameters empirically taken as $\alpha = -0.5$, $\beta = 1.5$ [23-25]. However, traditional Bruggeman equation is an empirical correlation based on sand medium permeability theory, which does not necessarily apply to oxygen diffusion process in the GDL with a small pore diameter, while accurately revealing oxygen diffusion characteristics in the GDL is necessary for PEMFC numerical simulations.

The traditional Bruggeman equation considers oxygen diffusion to be related only to the average porosity of porous media and average liquid water saturation, ignoring the influences of pore size and liquid water distribution. In recent years, some scholars had found that using the traditional Bruggeman equation to predict effective oxygen diffusion coefficient in the GDL, when taking $\alpha = -0.5$, $\beta = 1.5$, the predicted accuracy of oxygen diffusion is poor [26, 27]. Other studies [28-30] had pointed out not only the average porosity and average liquid water saturation, but also the pore size distribution and liquid water saturation distribution, affecting the effective oxygen diffusion coefficient in the GDL. In order to accurately predict effective oxygen diffusion coefficient, scholars had done lots of theoretical and experimental researches [31-33], focusing on the modification of two main parameters affecting effective oxygen diffusion coefficient α and β . A three-dimensional pore network model was used by Wu et al. [34] to determine the effective oxygen diffusivity in the GDL, where parameters were empirically taken as $\beta = 2.6$. Martínez-Rodríguez et al. [35] performed complementary characterizations for GDL by using scanning electron microscopy (SEM) images, pore size distribution (PSD) and fuel cell performance, in which parameters were empirically taken as $\alpha = -2.8$, $\beta = 3.8$. A pore network model of GDL is developed and validated by Gostick et al. [36], and the model idealized GDL as a regular cubic network of pore bodies following respective size distributions, where $\beta = 5.0$ was used in this study. As can be seen that the range of α given by these models is currently $-0.5 \sim 3.0$, and the range of β is $1.5 \sim 5.0$, but the values of α and β are still controversial.

Wang and Wang [37] used the principle of galvanic cells to design an experimental measuring device for effective oxygen diffusion coefficient in the GDL. The device can accurately measure effective oxygen diffusion coefficient in the dry GDL and the aqueous GDL. Experimental results indicate that effective oxygen diffusion coefficient predicted by the traditional Bruggeman equation is much higher than actual situation. Therefore, the traditional Bruggeman equation cannot be used to accurately quantify the performance of PEMFC. The influences of pore size distribution and liquid water distribution must be considered when predicting the oxygen diffusion coefficient in the GDL. For the GDL made of carbon paper, when the functions of pore size distribution and liquid water distribution are lacking, the approximate prediction can be made by further modifying parameter α and β in the Bruggeman equation, with the modification values of $\alpha = -3.0$ and $\beta = 4.0$ respectively. Therefore, the modified Bruggeman equation can be shown by:

$$D_{ij}^{eff} = D_{ij} (\varepsilon_i^{eff})^4 \quad (30)$$

Table 1. Source terms

Source terms	Unit	Domain
$Q_m = M_{O_2} Q_{O_2}^g + M_w S_w^v$	$\text{kg m}^{-3} \text{s}^{-1}$	GDL and CL
$R_{O_2} = -\frac{j}{4F}$	$\frac{\text{mol m}^{-3}}{\text{s}^{-1}}$	CL
$R_{H_2O} = \frac{j}{2F}$	$\frac{\text{mol m}^{-3}}{\text{s}^{-1}}$	CL
$S_w^{vl} = \begin{cases} k_{con} \frac{\varepsilon(1-s)x_w^g}{RT} (x_w^g p^g - p_{sat}) & x_w^g p^g \geq p_{sat} \\ k_{eva} \frac{\varepsilon s \rho_w^l}{M_w} (p_{sat} - x_w^g p^g) & x_w^g p^g < p_{sat} \end{cases}$	$\frac{\text{mol m}^{-3}}{\text{s}^{-1}}$	GDL and CL

Note: k_{con} and k_{eva} are condensation rate and evaporation rate respectively.

Table 2. Conservation of water in vapor, dissolved and liquid phases

Unit ($\text{mol m}^{-3} \text{s}^{-1}$)	CL	GDL
Water vapour S_w^v	$-S_w^{vd} - S_w^{vl}$	$-S_w^{vl}$
Liquid water S_w^l	$S_w^{dl} + S_w^{vl}$	S_w^{vl}
Dissolved water S_w^d	$S_w^{vd} - S_w^{dl}$	0

Note: superscripts meaning : *v* (vapor), *l* (liquid), *d* (dissolved), *vl* (vapour to liquid), *vd* (vapour to dissolved), *dl* (dissolved to liquid).

2.5. Boundary conditions and numerical solution

The water content on the CL-membrane interface is defined as the Dirichlet boundary with the value according to Eq. (13). The liquid water saturation at the inlet is also defined as the Dirichlet boundary with the value of zero. The inlet boundary conditions of each component are given by Eq. (31) ~ Eq. (33). Main parameters of numerical simulation are shown in Table 3.

$$x_{H_2O,in} = \frac{p_{sat} RH}{p} \tag{31}$$

$$x_{O_2,in} = 0.21(1 - x_{H_2O,in}) \tag{32}$$

$$x_{N_2,in} = 0.79(1 - x_{H_2O,in}) \tag{33}$$

In this study, multi-physics coupling analysis software COMSOL Multiphysics5.4 is used to solve the numerical model. The numerical solution of all equations is based on the finite element method (FEM). The meshing method uses a structured method and encrypts the thickness direction of GDL and CL. The calculation domain consists of 2,250 elements, and all the calculation models have been verified by grid independence.

Table 3. Physical parameters and properties

Symbol	Definition	Value
Physical constant and properties		
F	Faraday's constant (C mol ⁻¹)	96,485
R	Universal gas constant (J mol ⁻¹ K ⁻¹)	8.314
M_{O_2}	Molar mass of oxygen (kg mol ⁻¹)	0.032
M_{N_2}	Molar mass of nitrogen (kg mol ⁻¹)	0.028
M_{H_2O}	Molar mass of water (kg mol ⁻¹)	0.018
μ_{O_2}	Dynamic viscosity of oxygen (Pa s)	2.34968×10 ⁻⁵
μ_{N_2}	Dynamic viscosity of nitrogen (Pa s)	2.03572×10 ⁻⁵
μ_{H_2O}	Dynamic viscosity of water vapor (Pa s)	3.54064×10 ⁻⁴
ρ_{Pt}	Density of Platinum (kg m ⁻³)	21,450
ρ_C	Density of Carbon (kg m ⁻³)	2000
σ_C	Conductivity of carbon phase (S m ⁻¹)	1000
Geometry properties (base case)		
d_{GDL}	Gas diffusion layer thickness (um)	250
d_{CL}	Catalyst layer thickness (um)	15
d_{ch}	channel width (mm)	1.0
d_{rib}	rib width (mm)	1.0
ε_{GDL}	Porosity of GDL	0.65
ε_{CL}	Porosity of CL	0.35
r_{agg}	Agglomerate radius (nm)	200
r_{Pt}	Platinum radius (nm)	5
δ_e	Thickness of Nafion layer coating agglomerates (nm)	15
Electrochemical properties		
α_c	Charge transfer coefficient	0.5
$c_{O_2}^{ref}$	Oxygen reference concentration(mol m ⁻³)	0.85
Pt^{eff}	Utilization rate of specific Pt surface area	0.6
$a_{Pt/C}^{eff}$	Effective specific area of the catalyst layer (m ⁻¹)	3.6×10 ⁵
m^{Pt}	Platinum loading (mg cm ⁻²)	0.4
i_0^{ref}	Exchange current densities (A m ⁻²)	0.075
H_{O_2}	Oxygen Henry's law constant	0.64
Operating conditions (base case)		
T	Operating temperature (K)	353
P	Operating pressure (Pa)	1.5×10 ⁵
RH	Cathode relative humidity	100%
x_{O_2}	Inlet oxygen mole fraction	0.14455
x_{H_2O}	Inlet water vapor mole fraction	0.31169
x_{N_2}	Inlet nitrogen mole fraction	0.54376

3. RESULTS AND DISCUSSION

3.1. Model verification

In order to verify the accuracy of the modified model in this study, polarization curves of the simulation (base case) under the same operating condition are compared with polarization curves of the single cell measured by experiment. Experiment conditions include working temperature at 80 °C, absolute pressure at 1.5 bar, and air is completely humidified, and hydrogen is not humidified, and stoichiometry of hydrogen and air are 1.5 and 2.5 respectively. The membrane electrode assembly ('CCM' MEA, including catalyst layers and proton exchange membrane) with thickness of 60 μm from W. L. Gore & Associates (GORE®PRIMEA®MEA) is used, and platinum loading is 0.4 mg cm^{-2} for cathode and 0.1 mg cm^{-2} for anode respectively. GDL adopts Toray (Toray Industries) carbon paper with a thickness of 250 μm .

The comparison between the polarization curves of the numerical simulation and experimental results is shown in Fig. 3. From the trend of polarization curves, it can be found that the numerical models have less difference at low current density, but there is a significant difference at medium and high current density, especially during concentration polarization. Obviously, the modified model in this study agrees better with experimental results compared to other numerical models, which verifies the reliability of the modified model. For fuel cell water management, it is necessary to focus on the distribution of liquid water at medium and high current density in order to find an effective solution to the 'flooding'. Since the modified model is more in line with the actual working conditions of PEMFC at medium and high current density, the numerical simulations in this study will mainly use the modified model for further researches.

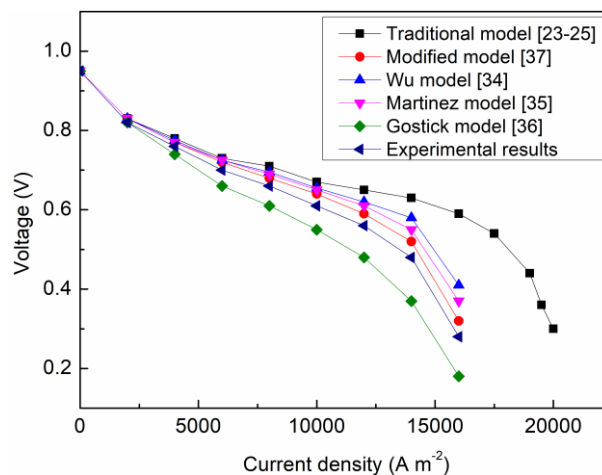


Figure 3. Comparison of simulation polarization curves and experimental results

3.2. Analysis of the relationship between liquid water and concentration polarization

At high current density, the concentration polarization of PEMFC is intensified, which is not beneficial to the improvement of power density. Increasing current density means more water generated,

and the water accumulation is closely related to concentration polarization. The further analysis made for this relationship is as follows. In order to facilitate the extraction of simulation results, three geometric coordinate points under rib are recorded as point 1, point 2, and point 3, respectively, and three geometric coordinate points under channel are respectively recorded as point 4, point 5, point 6, as shown in Fig. 4.

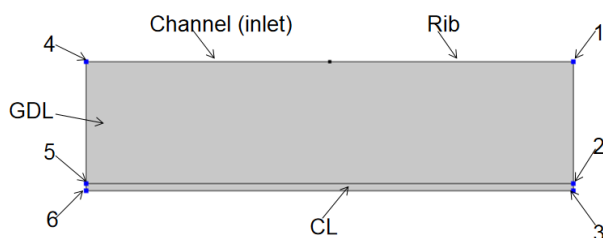
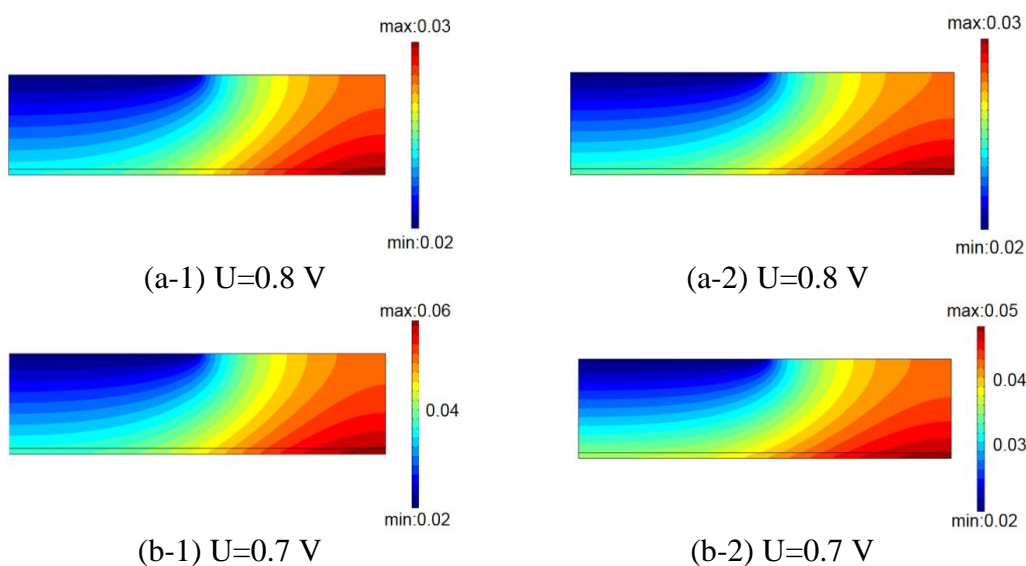


Figure 4. Geometric model of numerical simulation

With fuel cell voltage (U) at 0.8 V, 0.7 V, 0.6 V and 0.5 V, liquid water saturation distribution in porous media is shown in Fig. 5. It can be seen that as the voltage decreases, that is, the current density increases, liquid water saturation in porous media keeps increasing, and the farther away from the inlet, the larger the liquid water saturation. As shown in Eq. (24), effective porosity decreases as liquid water saturation increases, when voltage decreases from 0.8 V to 0.5 V, maximum liquid water saturation of the modified model increased by about 3.7 times, and effective porosity of GDL decreased by 8.2%. Compared with the modified model, numerical results of the traditional model are obviously larger in liquid water saturation, and the lower the voltage is, the larger the deviation of liquid water saturation will be.



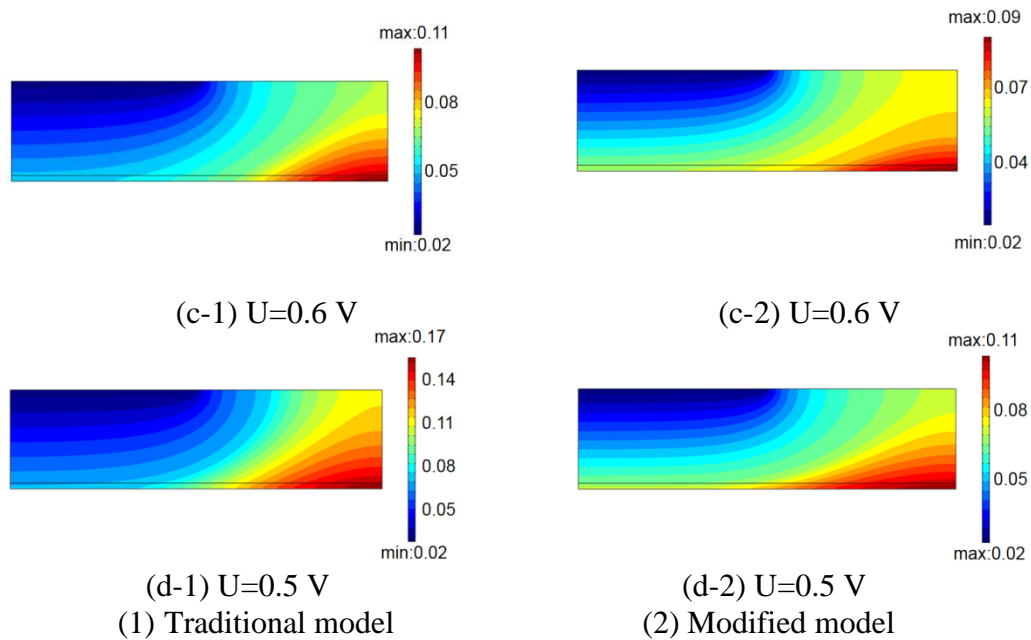


Figure 5. Liquid water saturation distribution in porous media with different voltages

The variation of the liquid water film thickness of the CL (point 5) is shown in Fig. 6. It is found that the liquid water film thickness of the CL predicted by different models shows obvious differences, and the smaller the value of β (or the absolute value of α) is, the greater the liquid water film thickness will be. This is because oxygen diffusion coefficient increases as β decreases according to the Bruggeman equation, which results in an increase in the electrochemical reaction rate and the generation rate of liquid water increases accordingly. As voltage decreases from 0.9 V to 0.1 V, water film thickness of the modified model increases from 1.3 nm to 6.3 nm. During concentration polarization, due to a large amount of liquid water covering the catalyst surface, the resistance of the oxygen transportation increases, resulting in a decrease in the electrochemical reaction rate and the generation rate of liquid water slows down accordingly. Therefore, the increased tendency of the water film thickness is flattened during concentration polarization. The oxygen concentration under rib at different locations is shown in Fig. 7. As the voltage decreases, the oxygen concentration in porous media drops rapidly, and the oxygen concentration maintains at a low level during concentration polarization. In addition, since porous media is clogged with liquid water, the further distance away from the inlet is, the lower the oxygen concentration will be.

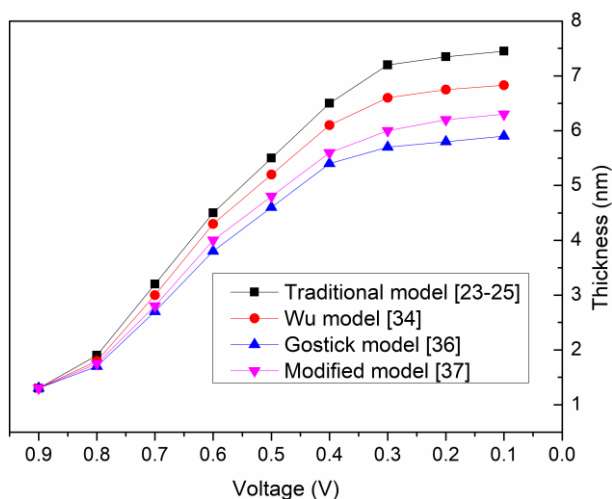


Figure 6. The variation of the liquid water film thickness of the CL

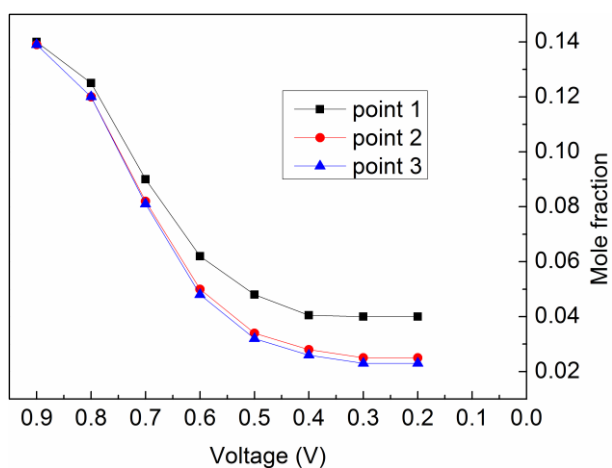


Figure 7. The oxygen concentration under rib at different locations

3.3. Liquid water distribution characteristics under different working conditions

When designing gas flow channels of PEMFC, the width of channel is often slightly larger than the width of rib. It can be seen from Fig. 5 that most of the liquid water is distributed under rib, and liquid water saturation under channel is lower. The rib obviously increases the resistance of the liquid water removed from porous media. Therefore, when designing the gas flow field, reducing the width of rib properly helps to enhance the capacity of liquid water discharge.

The comparison of liquid water saturation of the modified model between under channel and under rib is shown in Fig. 8. As the voltage drops, the growth rate of liquid water saturation under rib is greater than that under channel. At low voltages, liquid water saturation under rib is about 1.4 times under channel, and the liquid water accumulates much more significantly under rib than under channel at a common working voltage of around 0.55 V, thus reducing the width of rib slightly can effectively prevent ‘flooding’ happening. The variation of oxygen concentration under channel and under rib is shown in Fig. 9. As the voltage drops, the oxygen concentration under rib decreases faster than that

under channel due to the restriction of rib on oxygen transportation. During concentration polarization, the oxygen concentration under rib only about 30% under channel. Meanwhile, it shows that the oxygen concentration in porous media predicted by the traditional Bruggeman equation is higher, which agrees well with the experimental results of Wang and Wang [37], and further confirms the reliability of the modified model.

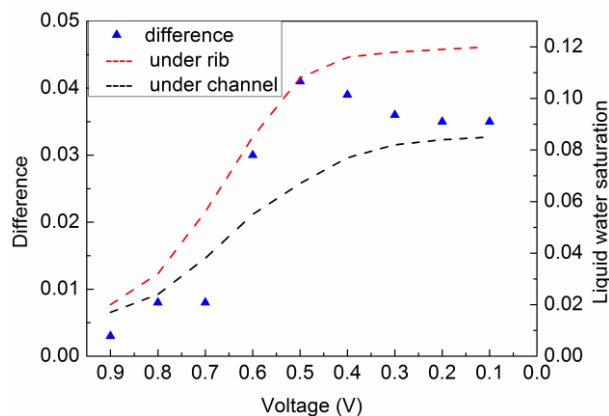


Figure 8. The comparison of liquid water saturation between under channel and rib

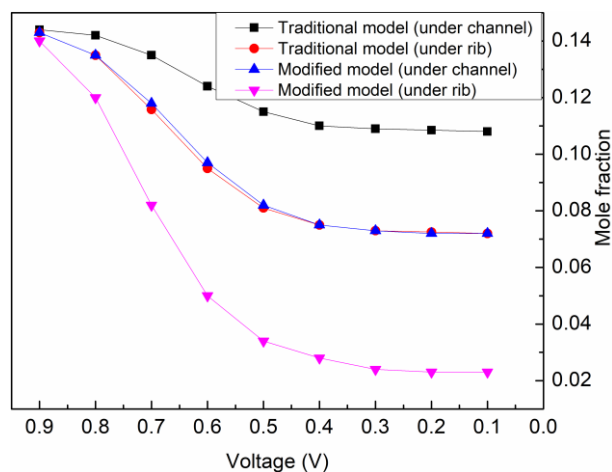


Figure 9. The variation of oxygen concentration under channel and rib

3.4. Influence of GDL structural characteristics on the liquid water distribution

3.4.1. Influence of GDL porosity on the liquid water distribution

The porosity and pore size are important parameters of GDL, which have important influences on the cell performance. Under the typical operating conditions with working voltage at 0.6 V, the comparison of liquid water saturation under channel and rib (point 5 and point 2, modified model) in porous media at different porosity is shown in Fig. 10. As the porosity decreases from 0.8 to 0.4, liquid water saturation under channel increases almost linearly, while liquid water saturation under rib

increases first and then decreases, showing a parabolic trend. When the porosity is 0.65, liquid water saturation under rib reaches maximum. Therefore, in order to ensure better performance of water discharge, GDL porosity should not be less than 0.65, and overall liquid water saturation is smaller at this time.

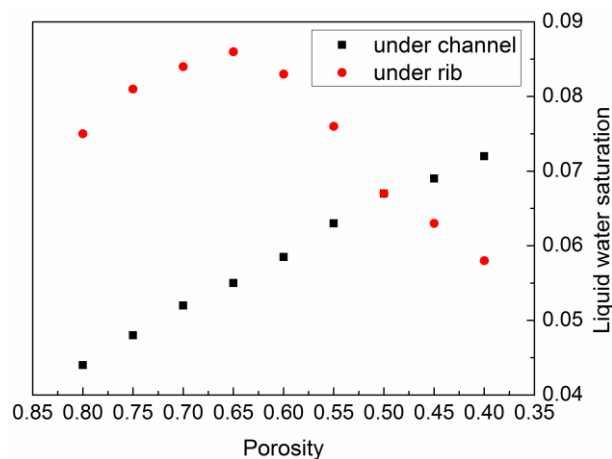


Figure 10. Liquid water saturation under channel and rib at different porosity

3.4.2. Influence of GDL pore size on the liquid water distribution

The pore structure of GDL is irregular. This study assumes that pore structure is round and pore size is the same, the pore size is 2.5 μm , 5.0 μm and 25 μm , respectively. The variation of the oxygen concentration of the modified model at different pore size (point 5) is shown in Fig. 11, and the variation of the liquid water saturation of different models at the corresponding position is shown in Fig. 12. It is found that pore size has little effect on oxygen transportation in porous media, while the smaller the pore size is, the larger the liquid water saturation will be, the more likely 'flooding' will occur. Therefore, GDL pore size should not be too small to prevent liquid water from blocking mass transfer channels. Meanwhile, it is also found that for different models, the smaller the value of β is, the greater the liquid water saturation will be, which is consistent with the changing trend of the liquid water film thickness of the CL in Fig. 6.

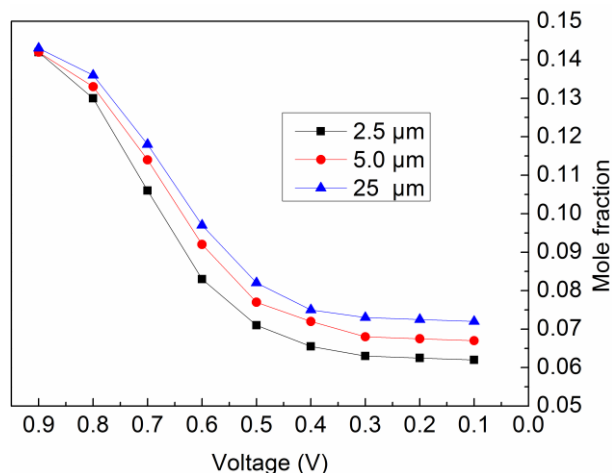


Figure 11. The variation of the oxygen concentration at different pore size

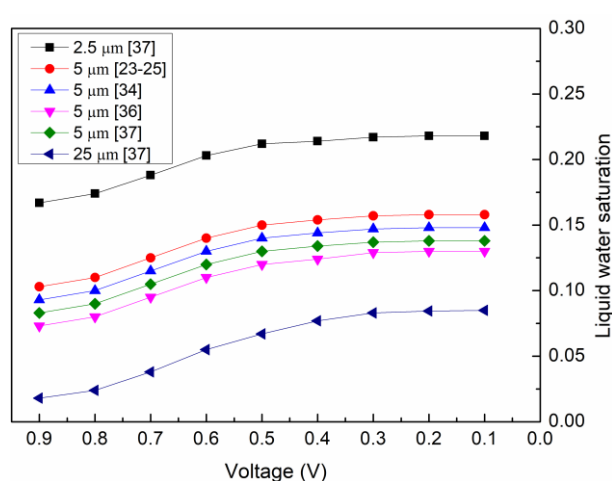


Figure 12. The variation of liquid water saturation at different pore size

3.4.3. Influence of GDL thickness on the liquid water distribution

GDL thickness has an important influence on mass transfer in porous media. In this study, GDL thickness is selected as 100 μm, 150 μm, 200 μm, 250 μm, and 300 μm, respectively. The variation of the oxygen concentration at the interface between GDL and CL under channel (point 5) is shown in Fig. 13, and the variation of the liquid water film thickness of the CL at the corresponding position is shown in Fig. 14. As the voltage decreases, thinner GDL thickness results in higher oxygen concentration at the interface. This is because thinner thickness brings out smaller resistance of the oxygen transportation through GDL and more oxygen reaching CL. It is also found that thinner GDL thickness results in thinner liquid water film thickness of the CL, which is beneficial to the removal of liquid water. Therefore, PEMFC optimized design should try to choose a thinner GDL.

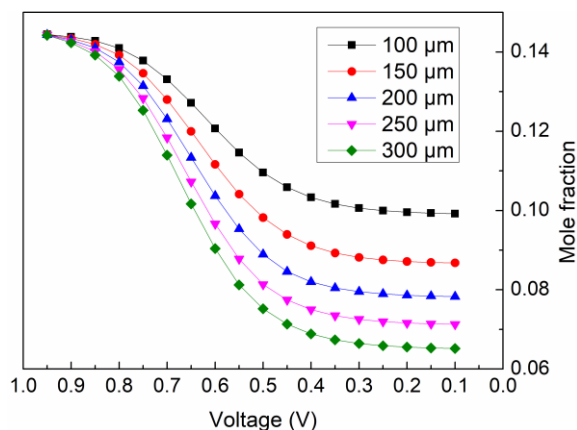


Figure 13. The variation of the oxygen concentration at the interface between GDL and CL under channel

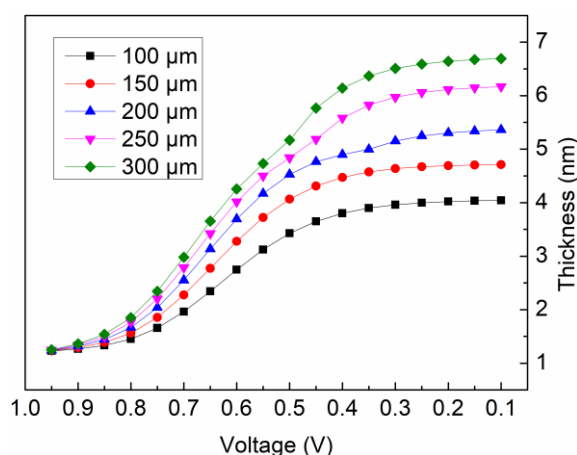


Figure 14. The variation of the liquid water film thickness of the CL

4. CONCLUSIONS

This study proposes a modified mass transfer model of cathode porous media, which modifies the traditional empirical value $\alpha = -0.5$, $\beta = 1.5$ of the Bruggeman equation for oxygen diffusion to $\alpha = -3.0$, $\beta = 4.0$. Combined with experimental verification, the reliability of the modified model is confirmed. Aiming at the liquid water distribution characteristics in porous media, the differences of numerical results between before and after modification are further compared, and the influences of various factors on the liquid water distribution are investigated. Conclusions are as follows:

(1) The numerical models have less difference at low current density, but there is a significant difference at medium and high current density, especially during concentration polarization. The modified model in this study agrees better with experimental results compared to other numerical models. The liquid water saturation and oxygen concentration predicted by the traditional Bruggeman equation are both higher, and the lower the voltage is, the larger the deviation will be. Meanwhile, Liquid water predicted by different models shows obvious differences, and the smaller the value of β (or the absolute value of α) is, the more the liquid water will be.

(2) The liquid water is accumulated and oxygen mass transfer resistance is enhanced due to increased current density. The reaction rate decreases during concentration polarization, and the generation rate of liquid water slows down accordingly. The farther distance away from the inlet is, the larger the liquid water saturation will be, and the lower the oxygen concentration will be. The growth rate of liquid water and the decrease rate of oxygen concentration under rib are larger than those under channel. The liquid water accumulates much more significantly under rib than under channel at a common working voltage of around 0.55 V, thus reducing the width of rib slightly can effectively prevent 'flooding'.

(3) As porosity of GDL decreases, liquid water under channel increases almost linearly, while liquid water under rib increases first and then decreases, exhibiting a parabolic trend. On the whole, liquid water is slightly saturated when porosity is greater than 0.65. The pore size has little influences on oxygen transportation, but smaller GDL pore size will considerably increase the risk of 'flooding'. The thinner GDL thickness is beneficial to the oxygen diffusion and the removal of liquid water. Therefore, in order to prevent 'flooding' of porous media area, GDL porosity should not be less than 0.65, and larger pore size and thinner thickness should be adopted appropriately.

ACKNOWLEDGEMENT

This work was supported by the National Key Research and Development Program of China (Heavy-Duty Truck Fuel Cell Engine Integration and Control). The authors would like to thank the editor and reviewers whose constructive and detailed critique contributed to the quality of this paper.

References

1. X. Zhou, Z. Niu, Y. Li, X. Sun, Q. Du, J. Xuan, and K. Jiao, *Int. J. Hydrogen Energy*, 44 (2019) 26498.
2. H. Liu, G. Zhang, D. Li, C. Wang, S. Bai, G. Li, and G. Wang, *Appl. Therm. Eng.*, 174 (2020) 115313.
3. X. Xie, G. Zhang, J. Zhou, and K. Jiao, *Int. J. Hydrogen Energy*, 42 (2017) 12521.
4. N. Djilali, and D. Lu, *Int. J. Therm. Sci.*, 41 (2002) 29.
5. A. Rowe, and X. Li, *J. Power Sources*, 102 (2001) 82.
6. K. J. Lee, J. H. Nam, and C. J. Kim, *Electrochim. Acta*, 54 (2009) 1166.
7. H. Sun, H. Liu, and L. J. Guo, *J. Power Sources*, 143 (2005) 125.
8. Y. Hou, G. Zhang, Y. Qin, Q. Du, and K. Jiao, *Int. J. Hydrogen Energy*, 42 (2017) 3250.
9. G. Zhang, and K. Jiao, *Energy Convers. Manage.*, 176 (2018) 409.
10. G. Zhang, H. Yuan, Y. Wang, and K. Jiao, *Appl. Energy*, 255 (2019) 1.
11. B. Xie, G. Zhang, J. Xuan J, and K. Jiao, *Energy Convers. Manage.*, 199 (2019) 1.
12. R. Banerjee, S. Chevalier, H. Liu, and J. Lee, *J. Electrochem. Energy*, (2017) 011002.
13. N. Ge, S. Chevalier, and J. Lee, *Int. J. Heat Mass Transfer*, 107 (2017) 418.
14. J. I. S. Cho, T. P. Neville, P. Trogadas, Q. Meyer, Y. Wu, R. Ziesche, P. Boillat, M. Cochet, V. Manzi-Orezzoli, P. Shearing, D. J. L. Brett, and M. O. Coppens, *Energy*, 170 (2019) 14.
15. G. Hu, G. Li, Y. Zheng, Z. Zhang, and Y. Xu, *J. Energy Inst.*, 87 (2014) 163.
16. L. Xing, M. Mamlouk, and K. Scott, *Energy*, 61 (2013) 196.
17. Y. Jiang, Z. Yang, K. Jiao, and Q. Du, *Energy Convers. Manage.*, 164(2018) 639.
18. W. He, *AIChE J.*, 46 (2000) 2053.

19. S. Mazumder, and J. V. Cole, *J. Electrochem. Soc.*, 150 (2003) A1503.
20. U. Pasaogullari, and C. Y. Wang, *Electrochim. Acta*, 49 (2004) 4359.
21. Y. Wang, and C. Y. Wang, *J. Electrochem. Soc.*, 153 (2006) A1193.
22. S. Mazumder, J. V. Cole, and *J. Electrochem. Soc.*, 150 (2003) A1503.
23. H. Meng, *J. Power Sources*, 168 (2007) 218.
24. T. F. Cao, H. Lin, L. Chen, Y. L. He, and W. Q. Tao, *Appl. Energy*, 112 (2013) 1115.
25. L. Xing, P. K. Das, X. Song, M. Mamlouk, and K. Scott, *Appl. Energy*, 138 (2015) 242.
26. N. Zamel, N. G. C. Astrath, X. Li, J. Shen, J. Zhou, F. B. G. Astrath, H. Wang, and Z. S. Liu, *Chem. Eng. Sci.*, 65 (2010) 931.
27. R. Vallabh, P. Banks-Lee, and A. F. Seyam, *J. Eng. Fibers Fabr.*, 5(2010) 7.
28. Y. Utaka, Y. Tasaki, S. Wang, T. Ishiji, and S. Uchikoshi, *Int. J. Heat Mass Transfer*, 52 (2009) 3685.
29. Z. Niu, B. Yang, H. Li, X. Li, and S. Wang, *Heat Transfer Eng.*, 35(2014) 1122.
30. P. A. García-Salaberri, J. T. Gostick, G. Hwang, A. Z. Weber, and M. Vera, *J. Power Sources*, 296 (2015) 440.
31. R. Wu, Q. Liao, X. Zhu, and H. Wang, *Int. J. Heat Mass Transfer*, 54 (2011) 4341.
32. J. Park, M. Matsubara, and X. Li, *J. Power Sources*, 173(2007) 404.
33. M. M. Mezedur, M. Kaviany, and W. Moore, *AIChE J.*, 48(2002) 15.
34. R. Wu, X. Zhu, Q. Liao, H. Wang, Y. D. Ding, J. Li, and D. D. Ye, *Electrochim. Acta*, 55 (2010) 7394.
35. M. J. Martínez-Rodríguez, T. Cui, S. Shimpalee, S. Seraphin, B. Duong, and J. W. V. Zee, *J. Power Sources*, 207 (2012) 91.
36. J. T. Gostick, M. A. Ioannidis, M. W. Fowler, and M. D. Pritzker, *J. Power Sources*, 173 (2007) 277.
37. S. X. Wang, and Y. L. Wang, *Int. J. Heat Mass Transfer*, 98 (2016) 541.

© 2020 The Authors. Published by ESG (www.electrochemsci.org). This article is an open access article distributed under the terms and conditions of the Creative Commons Attribution license (<http://creativecommons.org/licenses/by/4.0/>).